Waste-Derived Magnetically Recoverable CaO/Metakaolinite/Fe_3O_4 Nanocomposite Catalyst for Efficient Biodiesel Production from Neem Oil

A. Nwokedi[1,2*], U. G. Akpan[1], M. A. Olutoye[1], P. E. Dim[1]

[1]Department of Chemical Engineering, Federal University of Technology, P.M.B. 65, Minna, Nigeria.
[2]Department of Chemical Engineering, Nasarawa state University, P.M.B 1022, Keffi, Nigeria.

ABSTRACT: The development of sustainable, low-cost, and recyclable heterogeneous catalysts remains a major challenge for large-scale biodiesel production from non-edible oils. In this study, a novel waste-derived, magnetically recoverable CaO/metakaolinite/Fe_3O_4 nanocomposite catalyst was synthesized using eggshell waste, Kutigi kaolin clay, and plant-mediated magnetite through combined impregnation and green synthesis routes. Structural and textural characterization by XRD, HRSEM, HRTEM, BET, FTIR, and DLS confirmed the formation of a crystalline nanoscale composite with enhanced surface area, uniform dispersion of basic CaO active sites, and strong magnetic responsiveness. The catalyst exhibited appreciable basicity (0.5 mmol g^{-1}; pH 8.1–8.7), enabling efficient transesterification of high free-fatty-acid neem oil. Process optimization using Box–Behnken response surface methodology demonstrated excellent model adequacy (R^2 = 0.98; Adj-R^2 = 0.96), achieving biodiesel conversion above 90 wt.% under optimal reaction conditions. Gas chromatography–mass spectrometry confirmed the formation of major fatty acid methyl esters. The produced biodiesel satisfied ASTM D6751 fuel specifications, with density of 890 kg m^{-3}, kinematic viscosity of 4.6 mm^2 s^{-1}, flash point of 126 °C, and cetane number of 52. Reusability studies revealed that the catalyst retained approximately 62 wt.% of its initial activity after seven successive cycles, facilitated by efficient magnetic recovery and structural stability. Engine performance evaluation indicated improved brake thermal efficiency for blends up to B20, along with reduced CO and NO_x emissions relative to conventional diesel. Overall, the developed magnetic nanocomposite catalyst provides a scalable, environmentally benign, and cost-effective platform for sustainable biodiesel production from non-edible feedstocks.

KEYWORDS: Magnetic nanocomposite catalyst; Waste-derived CaO; Metakaolinite support; Neem oil biodiesel; Catalyst reusability; Sustainable biofuels.

[Received Jan. 30, 2026; Revised Mar. 03, 2026; Accepted Mar. 24, 2026] Print ISSN: 0189-9546 | Online ISSN: 2437-2110

I. INTRODUCTION

The increasing demand for sustainable and low-carbon energy alternatives has intensified global interest in biodiesel as a renewable substitute for petroleum-derived diesel fuels. Biodiesel offers several advantages, including biodegradability, reduced greenhouse gas emissions, and compatibility with existing compression ignition engines without major modifications (Long *et al.*, 2021; Sales *et al.*, 2022). However, large-scale biodiesel deployment remains constrained by high production costs, feedstock competition with food resources, and catalyst-related challenges, particularly during transesterification of low-cost, non-edible oils (Nabgan *et al.*, 2022; Linganiso *et al.*, 2022). Among heterogeneous catalysts, calcium oxide (CaO) derived from biogenic wastes such as eggshells, oyster shells, and animal bones has emerged as a promising low-cost alternative due to its strong basicity and catalytic activity (Naik *et al.*, 2024; Nguyen *et al.*, 2021). Numerous studies have reported high biodiesel yields using eggshell-derived CaO for various feedstocks, including neem oil, jatropha oil, waste cooking oil, and animal fats (Jeyakumar & Pandian, 2022; Iyya *et al.*, 2024; Erchamo *et al.*, 2021). Recent efforts have further explored CaO nanostructuring to enhance surface area and catalytic efficiency (Agnihotri *et al.*, 2024; Rahmayanti *et al.*, 2024). Despite these advances, conventional CaO-based catalysts still suffer from several critical limitations: (i) low surface area and particle agglomeration, (ii) poor structural stability and leaching during repeated use, and (iii) difficult recovery from reaction media, which collectively limit long-term industrial applicability (Saleem *et al.*, 2022; Abo & Areti, 2025).

To overcome these challenges, catalyst modification strategies such as metal doping, composite formation, and support immobilization have been investigated. Clay minerals, particularly metakaolinite, have attracted attention as catalyst supports due to their thermal stability, tunable porosity, and ability to disperse active sites while suppressing CaO sintering and leaching (Çakırca & Akın, 2021; Paredes-Quevedo *et al.*, 2025). However, most CaO–clay systems reported in the

*Corresponding author: minatnwokedi8888@gmail.com
doi: http://dx.doi.org/10.63746/njtd.v23i1.4403

literature focus primarily on yield optimization, with limited attention to nanoscale structural characterization, structure activity relationships, and catalyst recovery mechanisms. In parallel, magnetic nanoparticles such as Fe_3O_4 have been widely employed in catalysis to enable facile magnetic separation and recyclability (Liu *et al.*, 2014; Salgado Mendoza *et al.*, 2018). Yet, the integration of magnetic functionality into CaO–clay biodiesel catalysts remain scarcely explored, particularly for non-edible oils like neem oil.

A critical analysis of existing studies reveals a clear research gap. Previous studies have focused on neem oil biodiesel investigations relying on single-component or lightly

modified CaO catalysts, limited research has addressed nanoscale characterization, lack magnetic recovery capability, and rarely combine catalyst performance evaluation with engine-level validation (Noreen *et al.*, 2021; Jeyakumar & Pandian, 2022; Iyya *et al.*, 2024).

As a result, the relationship between catalyst structure, stability, recoverability, and real-world fuel performance remains insufficiently understood. Addressing this gap is essential for advancing waste-derived heterogeneous catalysts from laboratory-scale demonstrations toward practical and scalable biodiesel production systems.

In this context, the present study reports the development of a waste-derived, multifunctional CaO/metakaolinite/Fe_3O_4 magnetic nanocomposite catalyst synthesized entirely from renewable and locally available resources, including eggshell waste, Kutigi kaolin clay, and plant-mediated magnetite. Unlike previously reported CaO-based catalysts, the proposed composite integrates three complementary functionalities within a single catalyst architecture: (i) strong basic CaO active sites for efficient transesterification, (ii) metakaolinite structural support to enhance surface area and suppress CaO deactivation, and (iii) Fe_3O_4 nanoparticles to enable rapid magnetic recovery and reusability. Comprehensive nanoscale characterization is employed to establish structure property relationships, while process optimization is performed using response surface methodology. Importantly, the catalytic system is further validated through long-term reusability studies and engine performance and emission analysis of neem oil biodiesel blends. This integrated approach provides a robust and scalable pathway for sustainable biodiesel production from non-edible feedstocks while addressing key limitations identified in prior studies.

II. THEORETICAL ANALYSIS

A. *Fundamental Chemistry of Transesterification*

Transesterification is a reversible reaction in which triglycerides react with a short-chain alcohol (typically methanol) to produce fatty acid methyl esters (FAME) and glycerol as a by-product. The overall reaction is expressed as:

$$\text{Triglyceride} + 3CH_3OH \rightleftharpoons 3RCOOCH_3 + \text{Glycerol} \quad (1)$$

where R represents long-chain fatty acid groups (C_{12}–C_{24}). This reaction proceeds through three consecutive reversible steps involving the formation of diglycerides (DG) and monoglycerides (MG) as intermediates before yielding glycerol (GL) (Zhang et al., 2022; El-Sherif et al., 2023).
The stepwise mechanism can be represented as:

$$TG \rightleftharpoons DG \rightleftharpoons MG \rightleftharpoons GL \quad (2)$$

Each step produces one mole of FAME, and the overall efficiency depends on reaction conditions such as catalyst type, methanol-to-oil ratio, and temperature (Sathiyamoorthi et al., 2024; Saleem et al., 2022).

B. *Heterogeneous Base-Catalyzed Mechanism (CaO-Based Catalysts)*

Heterogeneous base catalysts, particularly CaO derived from waste materials such as eggshells, have gained significant attention due to their strong basicity, low cost, and environmental compatibility (Iyya et al., 2024; Agnihotri et al., 2024). The catalytic mechanism involves surface-mediated reactions occurring on basic sites (O^{2-} ions) and proceeds through the following steps:

i. Methanol activation: Surface basic sites abstract a proton from methanol to form methoxide ions
ii. Nucleophilic attack: Methoxide ions attack the carbonyl carbon of triglycerides.
iii. Intermediate formation: A tetrahedral intermediate is formed.
iv. Product formation: Collapse of the intermediate yields FAME and diglyceride.

This cycle continues until complete conversion to glycerol is achieved (Jeyakumar & Pandian, 2022; Nabgan et al., 2022).

C. *Mechanism of CaO/Metakaolinite/Fe_3O_4 Nanocomposite Catalyst*

The developed nanocomposite catalyst integrates CaO, metakaolinite, and Fe_3O_4 to achieve enhanced catalytic performance through synergistic interactions.

1. Synergistic Catalytic Effect

The incorporation of metakaolinite improves dispersion and stability of CaO active sites, while also introducing weak acidic sites that facilitate esterification of free fatty acids (FFA), making the catalyst bifunctional (Abo & Areti, 2025; Parveen & Bais, 2025).

2. Magnetic Recovery Function

The Fe_3O_4 component imparts magnetic properties, enabling efficient catalyst separation using an external magnetic field, thereby reducing downstream processing costs and catalyst loss (Rahmayanti et al., 2024; Awogbemi et al., 2024). In Figure 1 transesterification mechanism follows a heterogeneous base-catalyzed pathway facilitated by CaO active sites. In the first step, surface oxygen anions (O^{2-}) deprotonate methanol to form reactive methoxide ions. These methoxide ions subsequently attack the carbonyl carbon of triglycerides, leading to the formation of a tetrahedral intermediate. The intermediate collapses to release fatty acid methyl esters (FAME) and diglycerides, which further

undergo similar reactions until glycerol is formed. Metakaolinite enhances catalyst performance by improving surface area and dispersion of CaO, while Fe_3O_4 introduces magnetic properties, enabling rapid catalyst recovery using an external magnetic field. This significantly reduces separation cost and improves reusability.

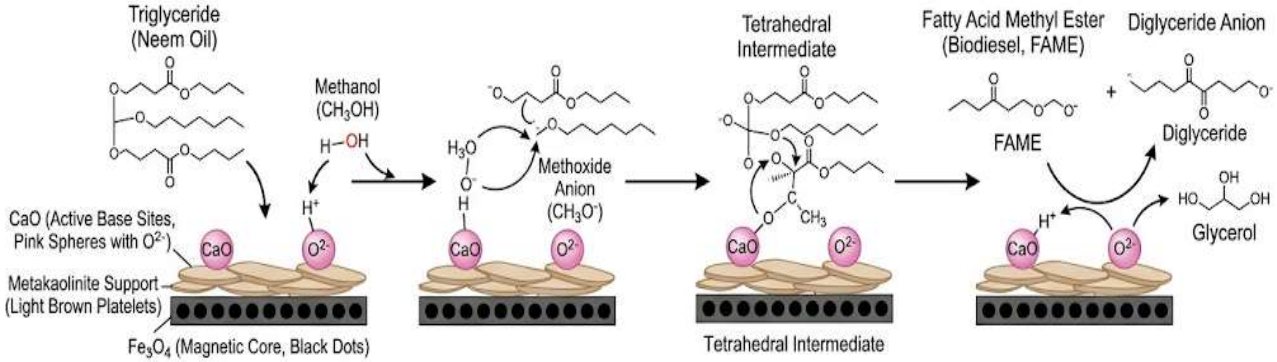

Figure 1 Mechanism of Transesterification over CaO/Metakaolinite/Fe_3O_4 Catalyst

D. Process Design for Biodiesel Production from Neem Oil

Neem oil is a non-edible feedstock characterized by relatively high free fatty acid (FFA) content (typically 5–20%), which necessitates pre-treatment prior to transesterification (Nguyen et al., 2021; Awogbemi et al., 2024). When FFA exceeds 2 wt.%, acid-catalyzed esterification is required:

$$RCOOH + CH_3OH \rightleftharpoons RCOOCH_3 + H_2O \quad (3)$$

This step reduces acid value and prevents soap formation during base-catalyzed transesterification (El-Sherif et al., 2023; Ulakpa et al., 2024).

E. Transesterification Process

The main reaction is carried out under moderate conditions using the synthesized nanocomposite catalyst. Typical operating conditions include:

i. Temperature: 60–65°C
ii. Methanol-to-oil ratio: 9:1–12:1
iii. Catalyst loading: 3–7 wt.%
iv. Reaction time: 2–4 hours

These parameters significantly influence biodiesel yield and conversion efficiency (Saleem et al., 2022; Sathiyamoorthi et al., 2024). After reaction completion, the mixture separates into two distinct phases:

i. Upper phase: Biodiesel (FAME)
ii. Lower phase: Glycerol and residual catalyst

Magnetic separation enables rapid recovery of the catalyst due to the presence of Fe_3O_4 nanoparticles, enhancing reusability and process sustainability (Rahmayanti et al., 2024; Nabgan et al., 2022). Figure 2 shows the Biodiesel production from neem oil involves a two-step process due to its high free fatty acid (FFA) content. Initially, crude oil undergoes pre-treatment (filtration and drying), followed by acid esterification to reduce FFA and prevent soap formation. The main transesterification reaction is then carried out using the CaO/metakaolinite/Fe_3O_4 nanocatalyst at moderate temperatures (60–65°C). Post-reaction, magnetic separation enables efficient catalyst recovery, after which the mixture separates into biodiesel and glycerol phases. The biodiesel is further purified through washing and drying to meet ASTM fuel standards. This integrated process ensures high efficiency, catalyst recyclability, and improved sustainability.

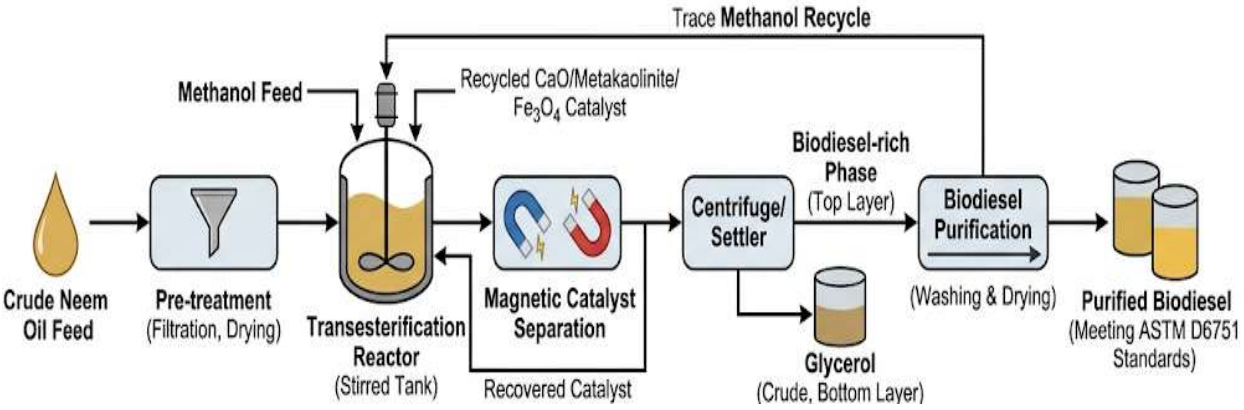

Figure 2 Process Flow Diagram for Biodiesel Production from Neem Oil

III METHODOLOGY

A. Materials and Reagents

Neem oil, used as a non-edible feedstock, was procured locally from Minna, Niger State, Nigeria. Eggshell waste, collected from eateries, was used as a calcium precursor for CaO synthesis (Naik *et al*., 2024; Saleem *et al*., 2022). Kaolin clay, obtained from Kutigi, Nigeria, was thermally activated to metakaolinite. Magnetite (Fe_3O_4) nanoparticles were synthesized via a green route using orange peel extract, selected based on its high phenolic content (Rehman *et al*., 2023; Salgado Mendoza *et al*., 2018). Analytical-grade methanol (≥99 wt.%) and all other chemicals including sodium hydroxide, ferric chloride, ferric nitrate, and concentrated sulfuric acid were used without further purification (Abo & Areti, 2025).

B. Catalyst Synthesis

1. Synthesis of Nano-Calcium Oxide

Eggshells were washed, inner membranes removed and dried at 105 °C for 12 h. Dried shells were pulverized, sieved through a 150 µm mesh, and ball-milled for 3 h to achieve a particle size of ~75 nm (Akatobi, 2024; Agnihotri *et al*., 2024). Calcination was performed at 900 °C for 2 h to convert $CaCO_3$ to CaO, with phase formation confirmed via XRD (El-Sherif *et al*., 2023). The thermal decomposition of calcium carbonate in eggshells into calcium oxide during calcination is represented by Equation (4), which explains the release of carbon dioxide and the formation of catalytically active CaO sites.

$$CaCO_{3(s)} \xrightarrow{900^oC} CaO_{(s)} + CO_{2(g)} \quad (4)$$

The conditions are as stated below:

i. Calcination temperature selected above the decomposition threshold of $CaCO_3$ (≥840 °C) to ensure complete phase transformation.
ii. Ball milling time optimized to balance particle size reduction and agglomeration prevention.

2. Synthesis of Nano-Metakaolinite

Raw kaolin clay was washed, dried at 80 °C for 12 h, and calcined at 750 °C for 2 h to produce metakaolinite (Rehman *et al*., 2023;). The material was ball-milled for 3 h to obtain ~98 nm particle size. Structural transformation was verified using XRD and FTIR. The structural dehydroxylation of kaolin to form amorphous metakaolinite upon thermal activation is described by Equation (5), highlighting the removal of hydroxyl groups essential for enhancing surface reactivity.

$$Al_2Si_2O_{5(s)}(OH)_4 \xrightarrow{750^oC} Al_2Si_2O_7 + 2H_2O \quad (5)$$

Considering the following criteria:

i. Calcination temperature chosen to induce dehydroxylation without sintering.
ii. Particle size maintained below 100 nm to enhance catalyst dispersion.

3. Green Synthesis of Magnetite (Fe_3O_4) Nanoparticles

Orange peel extract was used as a reducing agent due to its high phenolic content, confirmed via phytochemical analysis (Salgado Mendoza *et al*., 2018). Aqueous solutions of $FeCl_3$ (0.01 M) and $Fe(NO_3)_3$ (0.004 M) were mixed in a 2:1 Fe^{3+}:Fe^{2+} ratio. The extract (20 mL) was added to the iron precursor at 80 °C under continuous stirring. Sodium hydroxide (1 M) was added dropwise to adjust pH to 9, inducing uniform magnetite nanoparticle precipitation. The product was filtered, washed, dried at 70 °C for 12 h, and calcined at 450 °C for 2 h (Liu *et al*., 2014; Awogbemi *et al*., 2024). The coprecipitation reaction leading to the formation of magnetite nanoparticles under alkaline conditions is expressed by Equation (6), demonstrating the stoichiometric interaction between iron ions and hydroxide species.

$$2Fe^{3+} + Fe^{2+} + 8OH^- \rightarrow Fe_3O_4 + 4H_2O \quad (6)$$

where

i. pH is maintained at 9 to favor Fe_3O_4 formation over hematite.
ii. Orange peel extract selected for polyphenol-mediated reduction and stabilization.

4. Preparation of CaO/ Metakaolinite/ Fe_3O_4 Nanocomposite

The composite was synthesized via wet impregnation: CaO, metakaolinite, and Fe_3O_4 were mixed in a 2:1:1 mass ratio with 50 mL distilled water, homogenized for 30 min, filtered, oven-dried at 100 °C for 5 h, and calcined at 650 °C for 2 h to ensure uniform dispersion and stability (Abo & Areti, 2025). To evaluate the effectiveness of CaO and Fe_3O_4 dispersion on the metakaolinite support, the dispersion index was estimated using Equation (7), where higher values indicate improved surface exposure of active sites.

$$\text{Dispersion Index} = \frac{BET_{\text{composite}}}{BET_{\text{support}}} \qquad (7)$$

where:

$BET_{\text{composite}}$ is the specific surface area of the synthesized catalyst ($m^2\ g^{-1}$) and BET_{support}= specific surface area of the metakaolinite support ($m^2\ g^{-1}$)

This ratio provides a relative measure of surface modification after active phase incorporation. The mass ratio of 2:1:1 (CaO:Fe_3O_4:metakaolinite) was selected to ensure a high density of basic active sites (from CaO) while maintaining magnetic recoverability (from Fe_3O_4). Calcination at 650 °C was adopted to achieve optimal CaO crystallinity while preventing sintering and preserving Fe_3O_4 magnetic properties, as supported by prior studies.

C. Catalyst Characterization

Characterization techniques include:

i. XRD for phase identification and crystallite size (El-Sherif *et al*., 2023).
ii. BET analysis for surface area, pore volume, and porosity (Ulakpa *et al*., 2024).
iii. HRSEM/HRTEM with SAED for morphology and nanoscale structure (Liu *et al*., 2014).
iv. EDX for elemental composition (Nguyen *et al*., 2021).
v. FTIR to identify functional groups (Abo & Areti, 2025).
vi. Basicity determined using Hammett indicators (phenolphthalein, bromothymol blue, methyl orange) to quantify weak, medium, and strong basic sites (mmol g^{-1}) (Çakırca & Akın, 2021; Sathiyamoorthi et al., 2024).

The average crystallite size of the synthesized nanomaterials was determined from XRD data using the Scherrer equation, presented in Equation (8), which relates peak broadening to nanoscale dimensions.

$$D = \frac{K\lambda}{\beta \cos\ \theta} \qquad (8)$$

where:

D= crystallite size (nm)

K= shape factor (dimensionless, typically ≈ 0.9 for spherical particles)

λ= X-ray wavelength (nm), obtained from Cu-Kα radiation

β= full width at half maximum (FWHM) of diffraction peak (radians)

θ= Bragg diffraction angle (degrees or radians)

$K = 0.9$ was selected based on standard practice for nanocrystalline materials and λ corresponds to the radiation source of the diffractometer used.

The Brunauer–Emmett–Teller (BET) equation, shown in Equation (9), was employed to calculate the specific surface area of the catalyst from nitrogen adsorption–desorption isotherms.

$$\frac{1}{V\left[\left(\frac{P_0}{P}\right)-1\right]} = \frac{C-1}{V_m C}\cdot\frac{P}{P_0} + \frac{1}{V_m C} \qquad (9)$$

where:

V= volume of gas adsorbed ($cm^3\ g^{-1}$)

P= equilibrium pressure of nitrogen (Pa or atm)

P_0= saturation pressure of nitrogen (Pa or atm)

V_m= monolayer adsorbed gas quantity ($cm^3\ g^{-1}$)

C= BET constant (dimensionless), related to adsorption energy

Nitrogen adsorption–desorption isotherms at liquid nitrogen temperature were used to determine surface area. The total basicity of the catalyst was quantified using Hammett indicator titration, with the concentration of basic sites calculated according to Equation (10).

$$\text{Basicity} = \frac{C \times V}{m} \qquad (10)$$

where:

C= concentration of titrant (mol L^{-1})

V= volume of titrant consumed (L)

m= mass of catalyst sample (g)

Basicity unit = mmol g^{-1}

This method quantifies the density of basic active sites responsible for transesterification.

D. Pre-treatment, Biodiesel Synthesis and Process Optimization:

Prior to the main reaction, the neem oil was first subjected to an acid-driven esterification process to lower its free fatty acid (FFA) content to 1.1% which is suitable for alkaline transesterification. This pre-treatment is important because raw neem oil usually contains high FFAs, which can lead to soap formation, hinder the reaction, and reduce biodiesel recovery. Once the FFA level was sufficiently reduced, the oil underwent transesterification under optimized conditions.

Transesterification was conducted in a 250 mL batch reactor equipped with a mechanical stirrer and reflux condenser. Initial conditions: 0.8 wt. % catalyst, methanol-to-oil molar ratio of 9:1, reaction temperature 55 °C, and reaction time 2 h (Noreen *et al*., 2021; Iyya *et al*., 2024). Process optimization was performed using Box–Behnken Design under Response Surface Methodology (RSM) to investigate the effect of four independent variables (Table 1)

Table 1 Procedure for Box–Behnken Design under Response Surface Methodology (RSM)

Factor	Range	Units	Levels (-1, 0, +1)
Catalyst loading	0.3–1.0	wt%	0.3, 0.65, 1.0
Methanol-to-oil ratio	6:1–12:1	mol/mol	6:1, 9:1, 12:1
Reaction temperature	50–65	°C	50, 57.5, 65
Reaction time	60–120	Min	60, 90, 120

Each run was performed in triplicate. Biodiesel yield was determined gravimetrically Equation (11):

$$\text{Yield (\%)} = \frac{\text{Weight of biodiesel}}{\text{Weight of oil used}} \times 100 \qquad (11)$$

where:

Weight of biodiesel (g)

Weight of oil used (g)

Statistical analysis was performed using Design-Expert® software to determine optimum conditions (Paiva Pinheiro Pires *et al*., 2023; Rahmayanti *et al*., 2024). The overall transesterification reaction converting triglycerides into fatty acid methyl esters (FAME) and glycerol in the presence of the synthesized catalyst is illustrated in Equation (12).

$$Triglyceride + 3MeOH \xrightarrow{Catalyst} 3\text{FAME} + \text{Glycerol} \qquad (12)$$

Figure 3 illustrates the overall methodological workflow adopted in this study, detailing the sequential steps involved in catalyst screening, reusability assessment, reaction parameter optimization, and catalyst characterization for biodiesel production. The figure provides a visual summary of the decision-based experimental pathway, beginning with the evaluation of the synthesized nano-CaO/metakaolinite/Fe_3O_4 composite catalyst based on minimum conversion efficiency and stability criteria, followed by process optimization and final performance evaluation.

The relationship between biodiesel yield and the process variables was modeled using a second-order polynomial equation under Response Surface Methodology, as expressed in Equation (13).

$$Y = \beta_0 + \sum \beta_i X_i + \sum \beta_{ij} X_i X_j + \sum \beta_{ii} X_i^2 \qquad (13)$$

where:

Y= predicted biodiesel yield (%)

β_0= intercept term

β_i= linear coefficients

β_{ij}= interaction coefficients

β_{ii}= quadratic coefficients

X_i, X_j= independent variables (e.g., catalyst loading, methanol ratio, temperature, time)

The adequacy of the developed statistical model was evaluated using the criteria summarized in Equation (14), ensuring acceptable goodness-of-fit, predictive capability, and signal-to-noise ratio.

$$R^2_{\text{adj}} > 0.9, \text{lack-of-fit } p > 0.05, \text{Adeq Precision} > 4 \qquad (14)$$

where:

R^2_{adj}= adjusted coefficient of determination (dimensionless)

p= probability value (dimensionless)

Adeq Precision = signal-to-noise ratio (dimensionless)

These thresholds ensure strong predictive capability and statistical reliability (Rahmayanti *et al*., 2024).

The processes are as stated:

i. Catalyst loading: Limited to ≤1 wt% to avoid soap formation.
ii. Methanol ratio: Excess methanol shifts equilibrium forward.
iii. Temperature: Maintained below methanol boiling point.
iv. Time: Optimized to maximize yield without reverse reaction

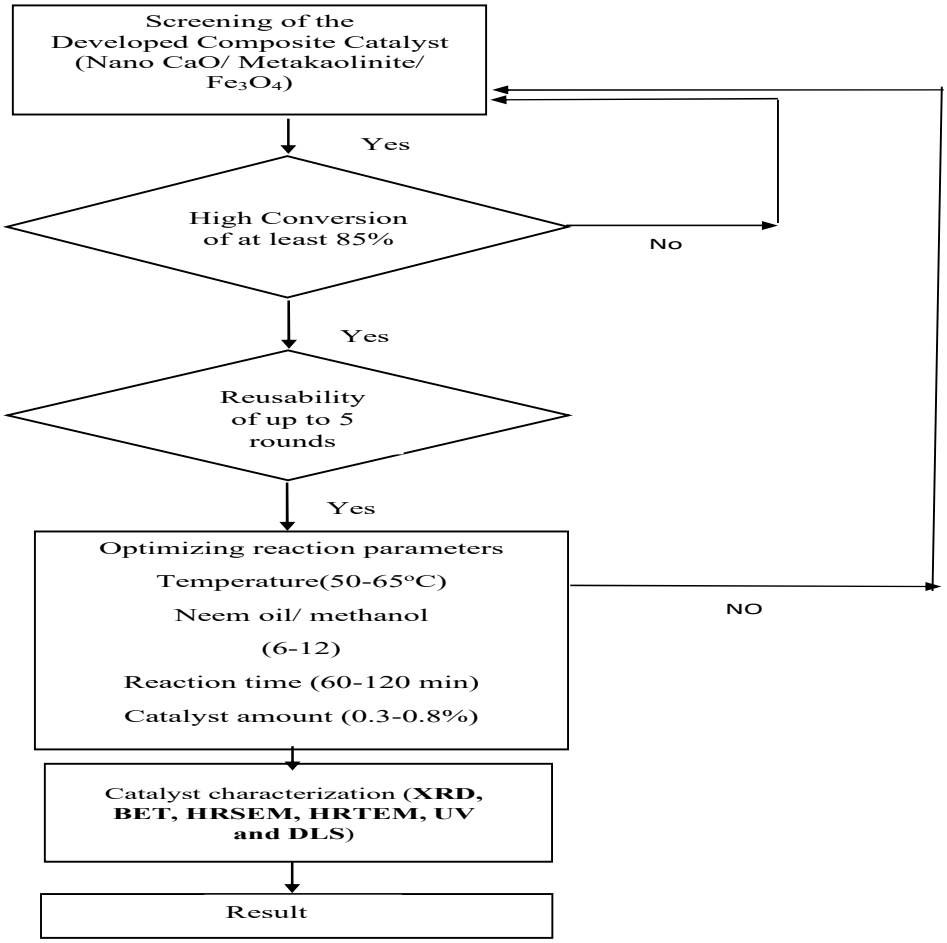

Figure 3 Methodological workflow for screening, optimization, and characterization of the nano-CaO/metakaolinite/Fe_3O_4 composite catalyst for biodiesel production.

E. Biodiesel Characterization

Physicochemical properties (density, viscosity, acid value, cetane number) were measured according to ASTM D6751. FAME composition was determined using GC–MS (Nguyen *et al*., 2021; Noreen *et al*., 2021). The kinematic viscosity of the produced biodiesel was determined using Equation (15), which relates efflux time to the viscometer calibration constant.

$$\nu = \frac{t}{C} \qquad (15)$$

where:

ν= kinematic viscosity ($mm^2\ s^{-1}$)

t= efflux time (s)

C= viscometer constant ($mm^2\ s^{-2}$)

The ignition quality of the biodiesel was estimated in terms of cetane index using the empirical relationship given in Equation (16), based on fuel density and boiling characteristics.

$$CI = 454.74 - 1641.416D + 774.74D^2 - 0.554B \qquad (16)$$

where:

- CI= cetane index (dimensionless)
- D= fuel density at 15 °C (g cm^{-3})
- B= distillation temperature at 50% recovery (°C)

Empirical correlation widely used for diesel fuel quality estimation (Noreen *et al*., 2021).

F. Catalyst Reusability and Magnetic Recovery

After each cycle, the catalyst was magnetically separated, washed with methanol and n-hexane, dried at 105 °C for 4 h, and reused for up to five cycles. Biodiesel yield was recorded for each cycle (Erchamo *et al*., 2021; Sathiyamoorthi *et al*., 2024). The reusability performance of the catalyst was quantified by calculating activity retention after successive cycles using Equation (17).

$$\text{Activity Retention (\%)} = \frac{Y_n}{Y_1} \times 100 \qquad (17)$$

where:

Y_n= yield at cycle n(%)

Y_1= yield at first cycle (%)

G. Engine Performance and Emission Analysis

Biodiesel blends (B20, B50, B100) were tested in a single-cylinder, 4-stroke compression ignition engine. Evaluated parameters included:

- Brake power (BP)

- Brake thermal efficiency (BTE)
- Brake specific fuel consumption (BSFC)
- Exhaust emissions: CO, NO_x, particulate matter

Fuel consumption was calculated as shown in Equation (18):

$$FCR = \frac{V}{t} \qquad (18)$$

where FCR is the fuel consumption rate (mL s^{-1} or L h^{-1}), V, the volume of fuel consumed (mL or L), t is the time (s or h). With operation across 1000–2000 rpm and varying loads (Linganiso *et al*., 2022; Long *et al*., 2021). Brake thermal efficiency, representing the effectiveness of converting chemical energy into mechanical output, was calculated using Equation (19).

$$BTE = \frac{BP}{\dot{m}_f \times LHV} \qquad (19)$$

where BTE is the brake thermal efficiency (%), BP, the brake power (kW), $\dot{m}_f$, the fuel mass flow rate (kg s^{-1}) and LHV is the lower heating value (MJ kg^{-1})

Fuel economy of the engine operating on biodiesel blends was evaluated using brake specific fuel consumption, as defined in Equation (20).

$$BSFC = \frac{\dot{m}_f}{BP} \qquad (20)$$

where $BSFC$ is the brake specific fuel consumption (kg kW^{-1} h^{-1}) and $\dot{m}_f$ is the fuel mass flow rate (kg h^{-1})

IV RESULTS AND DISCUSSION

A. Raw Material and Catalyst Support Characterization

The XRF results presented in Table 2 indicate that Kutigi kaolin is predominantly composed of SiO_2 (57.99 wt.%) and Al_2O_3 (33.24 wt.%), confirming its classification as a silica–alumina–rich clay, which is a desirable characteristic for catalyst support applications. The high SiO_2–Al_2O_3 framework provides structural rigidity, thermal stability, and surface hydroxyl groups that facilitate effective anchoring and dispersion of active catalytic phases, particularly metal oxides and basic sites. Similar compositional profiles have been reported for kaolinite-based supports successfully employed in heterogeneous catalysis and biodiesel-related reactions (Nguyen *et al*., 2021; Paredes-Quevedo *et al*., 2025).

The presence of minor oxides such as TiO_2 (3.43 wt.%) and Fe_2O_3 (2.71 wt.%) is advantageous, as these species can enhance surface acidity–basicity balance and contribute to improved interfacial interactions between the support and deposited CaO and Fe_3O_4 phases. Importantly, the very low CaO content (0.42 wt.%) in the raw clay confirms that catalytic basicity is not inherent to the support but is deliberately introduced through waste-derived CaO loading, thereby allowing controlled tuning of active sites. This approach aligns with current strategies in heterogeneous biodiesel catalysis that emphasize support inertness combined with externally introduced basic functionality (Abo & Areti, 2025; Awogbemi *et al*., 2024). Trace elements (e.g., ZnO, BaO, Cr_2O_3, Nb_2O_3) were detected only at negligible levels (<0.1 wt.%), indicating minimal impurity interference and reducing the likelihood of catalyst poisoning or undesirable side reactions during transesterification. Overall, the chemical composition of Kutigi kaolin demonstrates its suitability as a locally sourced, low-cost, and structurally stable support for the development of sustainable nanocomposite catalysts, reinforcing its relevance to biodiesel production systems based on waste-derived active components (Nabgan *et al*., 2022; Paredes-Quevedo *et al*., 2025).

Table 2 Chemical Composition of Kutigi Kaolin (XRF Analysis)

Component	Concentration (wt.%)	Component	Concentration (wt.%)
SiO_2	57.987	ZnO	0.008
Al_2O_3	33.237	BaO	0.060
TiO_2	3.427	P_2O_5	0.100
Fe_2O_3	2.709	Cr_2O_3	0.036
CaO	0.417	V_2O_5	0.182
K_2O	0.671	Ta_2O_5	0.027
SO_3	0.138	Ag_2O	0.034
Cl	0.621	MnO	0.038
ZrO_2	0.224	Nb_2O_3	0.017
CUO	0.057	Total	100

B. Textural Properties of Synthesized Catalysts

The nitrogen adsorption–desorption isotherms of nano-CaO, nano-metakaolinite, and the CaO/Metakaolinite/Fe_3O_4 nanocomposites (Figure 4(a and b)) exhibit Type IV(a) isotherms with pronounced H3 hysteresis loops, according to IUPAC classification. This behavior is characteristic of

mesoporous materials with slit-shaped pores, typically arising from the aggregation of plate-like particles, a structural feature commonly reported for clay-derived catalyst supports such as metakaolinite (Paredes-Quevedo *et al*., 2025; Nabgan *et al*., 2022). The mesoporous architecture is particularly advantageous for heterogeneous transesterification, as it facilitates reactant diffusion while maintaining high surface accessibility to basic active sites (Awogbemi *et al*., 2024).

As summarized in Table 3, nano-metakaolinite exhibits a substantially higher BET surface area (114 $m^2\ g^{-1}$) than nano-CaO (60.05 $m^2\ g^{-1}$), reflecting the intrinsic layered aluminosilicate structure of the support. Upon incorporation of CaO and Fe_3O_4, all nanocomposite formulations demonstrate enhanced surface areas (109–117 $m^2\ g^{-1}$) and increased pore volumes (0.78–0.89 $cm^3\ g^{-1}$) relative to pristine CaO. This improvement indicates that dispersing CaO and magnetite within the metakaolinite matrix effectively suppresses CaO particle agglomeration, a known limitation of unsupported CaO nanocatalysts (Agnihotri *e al*., 2024; Nguyen *et al*., 2021). Stoichiometric variation markedly influences pore structure development. The CaO-rich formulation (2:1:1) achieves the highest BET surface area (117 $m^2\ g^{-1}$) and the largest average pore diameter (3.5 nm), suggesting that increased CaO loading promotes pore widening within the composite framework. Conversely, higher Fe_3O_4 content (1:1:2) primarily enhances pore volume, likely due to magnetite-induced interparticle spacing within the clay matrix. Similar trends have been observed in clay-supported and biogenic CaO-based nanocatalysts, where controlled metal oxide dispersion generates hierarchical mesoporosity favorable for biodiesel reactions (El-Sherif *et al*., 2023; Saleem *et al*., 2022).

Overall, the combined increase in surface area, mesopore volume, and pore diameter confirms that the CaO/Metakaolinite/Fe_3O_4 nanocomposites possess textural properties optimized for heterogeneous biodiesel catalysis. These features are expected to enhance catalytic efficiency by maximizing accessible basic sites while minimizing internal mass-transfer resistance during triglyceride transesterification, in line with current design principles for advanced solid base catalysts (Nabgan *et al*., 2022). Volume from 0.80 to 0.01132 cm^3/g. This is consistent with the deactivation of biodiesel catalysts, where there is pore blockage due to glycerol, soaps, and unreacted substances (Fronza et al., 2026). The same findings have been reported by other studies, where there is significant fouling, calcium leaching, and pore size reduction, resulting in a significant reduction of surface area and efficiency after repeated biodiesel synthesis cycles. Percentages (Suhel et al., 2025).

As shown from the reduction of pore widths from 3.5 to 2.042 nm, there is a significant indication of the transition to restricted diffusion, as shown by textural degradation rather than chemical deactivation.

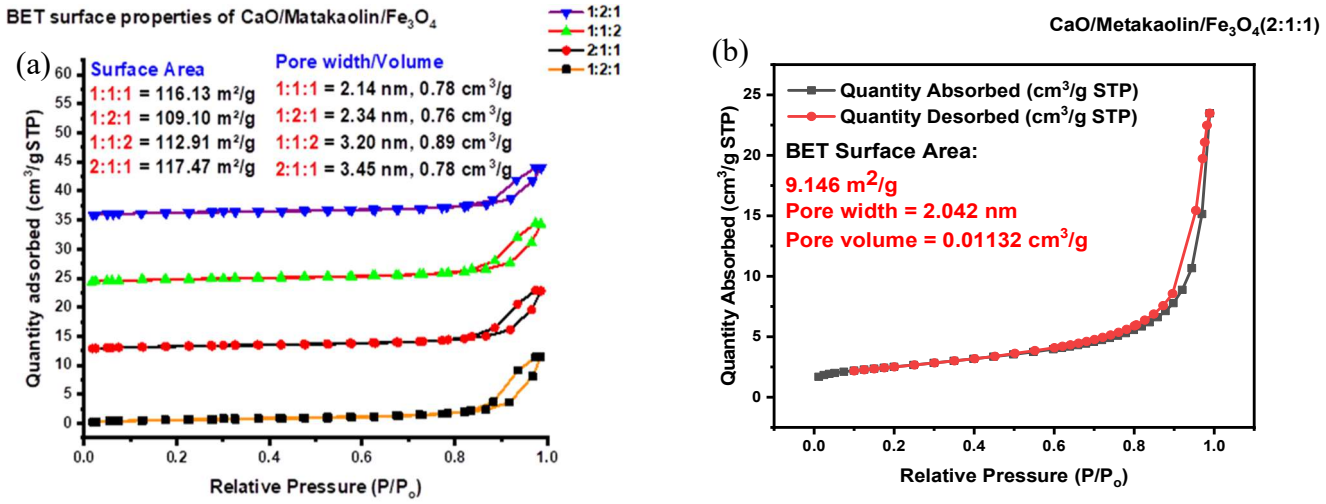

Figure 4 (a) N_2 Adsorption–Desorption Isotherms of the Nanocomposite Catalyst (b). N_2 Adsorption–Desorption Isotherms of spent 2:1:1 Nanocomposite Catalyst

Table 3 BET Surface Properties of CaO, Metakaolinite, Fe_3O_4, and CaO/Metakaolinite/Fe_3O_4 Nanocomposite

	Nano CaO	Nano MK	Nano CKM111	Nano CKM121	Nano CKM112	Nano CKM211
BET surface area (m^2/g)	60.05	114	116	109	112	117
Pore volume (cm^3/g)	0.50	0.70	0.78	0.78	0.89	0.80
Pore diameter (nm)	3.0	2.9	2.4	2.2	3.2	3.5

C. Structural and Phase Analysis

X-ray diffraction (XRD) analysis (Figure 5) confirms the successful phase transformation, crystallinity retention, and effective integration of CaO and Fe_3O_4 within the metakaolinite matrix. The raw kaolin exhibits sharp basal reflections characteristic of an ordered kaolinite structure, which completely disappear after calcination, giving rise to a broad amorphous halo in the 2θ range of 20–30°, evidencing full dehydroxylation and conversion to highly reactive metakaolinite. This structural amorphization is essential for enhancing metal dispersion and interfacial contact in clay-based catalyst supports, as widely reported for metakaolin-derived composites (Abo & Areti, 2025; Awogbemi *et al*., 2024).

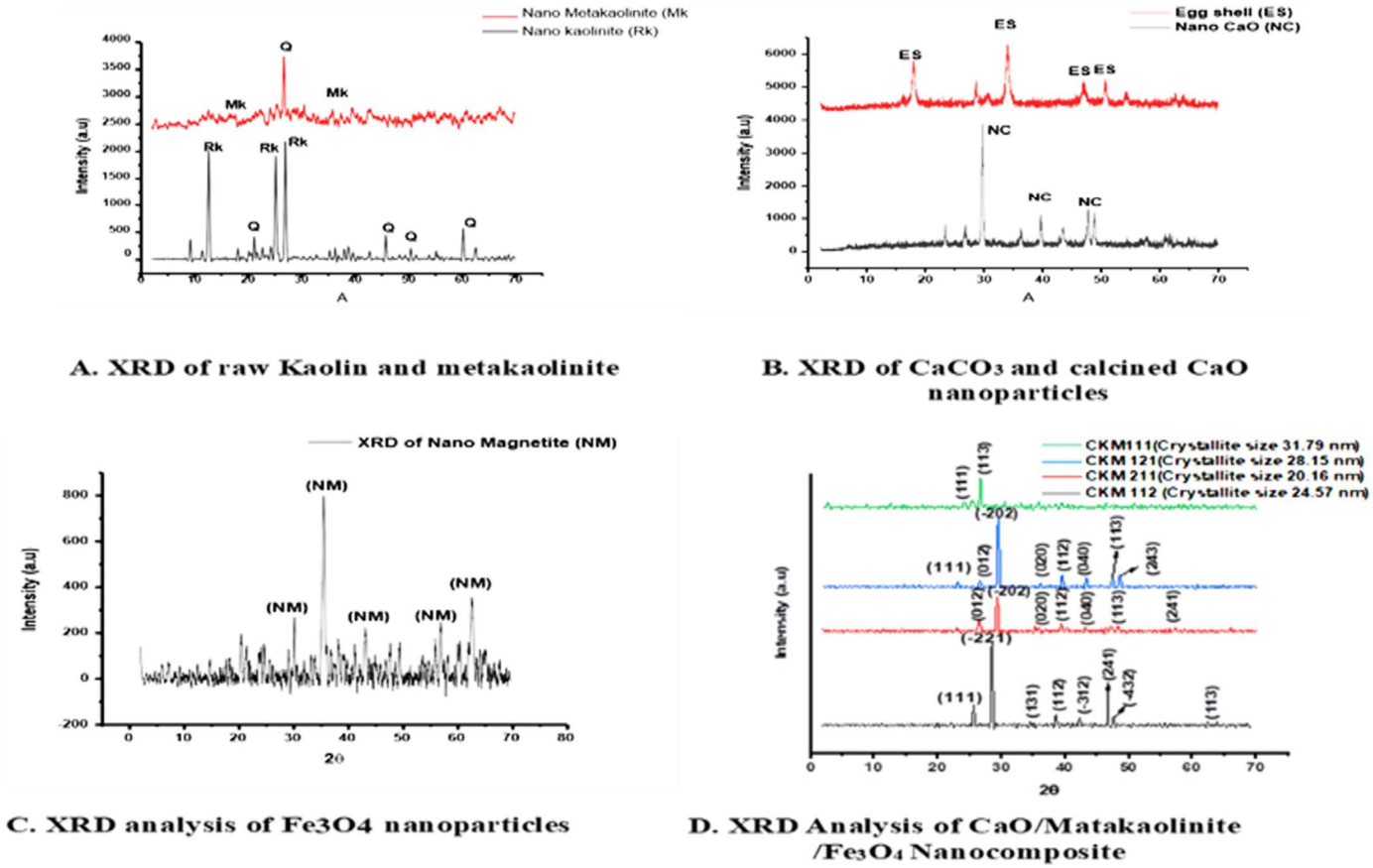

Figure 5 XRD Patterns of Raw Kaolin, Metakaolinite, CaO, Fe_3O_4, and CaO/Metakaolinite/Fe_3O_4 Nanocomposite

The nanocomposite diffractogram shows well-defined reflections corresponding to cubic spinel Fe_3O_4 and crystalline CaO superimposed on the amorphous metakaolinite background, confirming the coexistence of all functional phases without the formation of undesirable secondary compounds. The absence of significant peak shifts indicates that CaO and Fe_3O_4 retain their intrinsic crystal structures and are physically anchored within the support rather than forming solid solutions, a feature favorable for preserving basicity and magnetic recoverability (Agnihotri *et al*., 2024; El-Sherif *et al*., 2023). Moreover, the moderate broadening of CaO reflections in the composite relative to pristine CaO suggests reduced crystallite size and suppressed sintering due to spatial confinement by the metakaolinite framework, consistent with reports on supported CaO nanocatalysts for biodiesel applications (Akatobi, 2024; Çakırca & Akın, 2021). Collectively, the XRD results demonstrate a structurally synergistic hybrid system, combining an amorphous, high-reactivity support with well-dispersed crystalline active phases suitable for heterogeneous catalysis.

D. Nanoscale Morphology and Microstructural Features

HRTEM and SAED analysis (Figure 6) provides direct nanoscale evidence of the structural integrity and phase dispersion within the CaO/Metakaolinite/Fe_3O_4 nanocomposite. High-resolution TEM micrographs reveal that CaO and Fe_3O_4 nanoparticles are homogeneously dispersed on the metakaolinite sheets, effectively preventing the agglomeration of magnetic Fe_3O_4 cores due to dipolar interactions. Lattice fringe measurements of 0.25 nm and 0.24 nm correspond to the (311) plane of Fe_3O_4 and the (200) plane of CaO, respectively, confirming the coexistence of both crystalline active phases

(Abo & Areti, 2025; Agnihotri *et al*., 2024; El-Sherif *et al*., 2023).

Selected area electron diffraction (SAED) patterns display well-defined concentric polycrystalline rings that can be indexed to the cubic structures of Fe_3O_4 and CaO, superimposed on the diffuse halo of the amorphous metakaolinite support. This observation corroborates the XRD results, indicating that the active phases maintain high crystallinity despite fine dispersion within the clay matrix, while the metakaolinite provides structural stabilization and enhanced interfacial contact, crucial for catalytic performance (Akatobi, 2024; Awogbemi *et al*., 2024; Çakırca & Akın, 2021). Collectively, the HRTEM and SAED analyses confirm the successful fabrication of a structurally robust and highly accessible nanocomposite architecture suitable for heterogeneous catalysis.

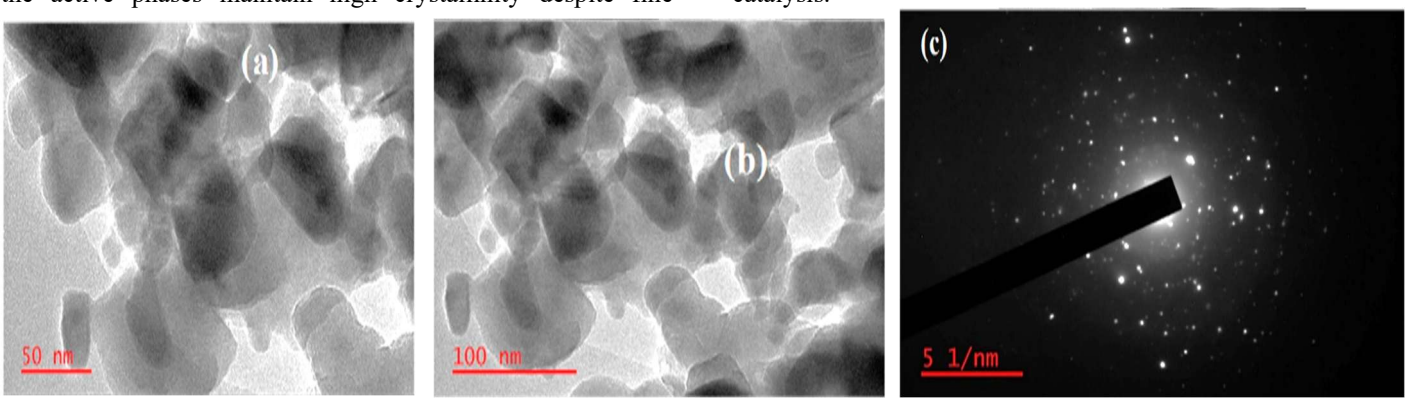

Figure 6 HRTEM and SAED Images of the CaO/Metakaolinite/Fe_3O_4 Nanocomposite

The VSM curve shown in Figure 7 has a typical S-shaped hysteresis loop with negligible coercivity and remanence, indicating the superparamagnetic nature of the CaO/metakaolin/Fe_3O_4 (2:1:1) nanocomposite material, which is necessary for rapid magnetic recovery. The obtained saturation magnetization value (Ms) is found to be lower than that of pure Fe_3O_4 (60–80 emu g^{-1}). This may be attributed to the dilution effect of non-magnetic CaO and metakaolin phases present in the composite material, which reduces the magnetization values while allowing for separability (Koo et al., 2019). This has been found to be true for magnetite-based composite materials, which retain their magnetic responsiveness despite having low values of Ms (de Jesus Andrade Fidelis et al., 2025).

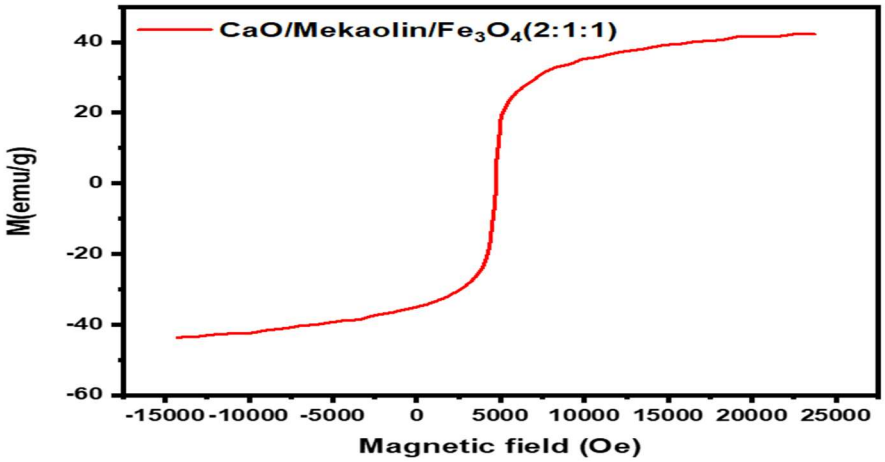

Figure 7 VSM hysteresis loop of the magnetic properties of CaO/Metakaolinite/Fe_3O_4 Nanocomposite (2:1:1)

E. Transesterification Optimization and Statistical Modeling

The Box–Behnken experimental design (Table 4) systematically evaluated the influence of catalyst loading, reaction temperature, time, and methanol-to-oil ratio on biodiesel yield using the CaO/Metakaolinite/Fe_3O_4 nanocomposite catalyst. The observed yields ranged from 81.42 wt.% to 93.93 wt.%, highlighting the sensitivity of the transesterification process to the selected operational parameters, consistent with trends reported for heterogeneous CaO-based nanocatalysts (Agnihotri *et al*., 2024; El-Sherif *et al*., 2023; Abo & Areti, 2025).

Statistical analysis (Table 5) confirms that a quadratic model best describes the relationship between process variables and biodiesel yield (R^2 = 0.9818, Adjusted R^2 = 0.9636, Predicted R^2 = 0.9444), with a non-significant lack-of-fit (p = 0.9758) and an adequate precision of 29.39, indicating excellent predictive capability. Catalyst loading, temperature, reaction time, and methanol-to-oil ratio were all significant individual

factors ($p < 0.0001$), while interaction terms such as AC, AD, BC, BD, and CD also influenced yield, demonstrating the synergistic effects of process variables on transesterification efficiency (Naik *et al*., 2024; Iyya *et al*., 2024; Awogbemi *et al*., 2024).

These results confirm that optimization of operational parameters is crucial to maximizing biodiesel yield, with the finely dispersed CaO/Fe_3O_4 nanoparticles on metakaolinite providing high catalytic activity, surface accessibility, and stability, in agreement with previous studies on biogenic and composite heterogeneous catalysts (Jeyakumar & Pandian, 2022; Akatobi, 2024; Çakırca & Akın, 2021). The parity plot (Figure 8) demonstrates excellent agreement between experimental and predicted biodiesel yields, with data points closely aligned along the 45° diagonal, indicating a high coefficient of determination ($R^2 > 0.95$). This strong correlation confirms that the quadratic response surface model is both precise and robust, with minimal experimental error, high predictive reliability, and no evidence of overfitting, as reflected in the high adjusted and predicted R^2 values (Agnihotri *et al*., 2024; El-Sherif *et al*., 2023; Abo & Areti, 2025).

Such reliable predictive performance is consistent with previous reports on CaO-based heterogeneous catalysts, where careful optimization and statistical modeling enable accurate forecasting of biodiesel yields under varying operational conditions (Naik *et al*., 2024; Iyya *et al*., 2024; Awogbemi *et al*., 2024). The tight clustering of points around the unit slope line further validates the model's capability to capture the interactions between catalyst loading, reaction temperature, time, and methanol-to-oil ratio, reinforcing the suitability of RSM and similar statistical approaches for designing efficient transesterification processes using nanocomposite catalysts (Jeyakumar & Pandian, 2022; Akatobi, 2024; Çakırca & Akın, 2021).

Table 4 Box–Behnken Experimental Design and Biodiesel Yield

Run	Catalyst Loading (wt. %)	Temperature (°C)	Time (min)	Methanol-to-Oil Ratio (mol)	Percentage Yield (wt.%)
1	0.55	57.5	90	9	86.85
2	0.30	50.0	90	9	87.09
3	0.80	50.0	90	9	90.73
4	0.80	57.5	90	6	91.79
5	0.30	57.5	90	6	81.42
6	0.55	57.5	90	9	84.85
7	0.55	65.0	60	9	83.98
8	0.30	65.0	90	9	82.47
9	0.80	57.5	120	9	93.93
10	0.55	50.0	120	9	91.41
11	0.55	50.0	90	6	85.66
12	0.55	65.0	120	9	89.98
13	0.55	57.5	90	9	86.85
14	0.55	50.0	90	12	91.71
15	0.55	65.0	90	6	86.15
16	0.30	57.5	60	9	85.60
17	0.55	57.5	90	9	86.85
18	0.55	57.5	120	6	92.48
19	0.55	50.0	60	9	89.91
20	0.80	57.5	90	12	87.88
21	0.30	57.5	120	9	88.85
22	0.55	57.5	60	12	90.60
23	0.55	57.5	60	6	84.23
24	0.55	65.0	90	12	83.86
25	0.30	57.5	90	12	89.09
26	0.55	57.5	90	9	86.85
27	0.55	57.5	120	12	89.85
28	0.80	57.5	60	9	87.62
29	0.80	65.0	90	9	87.99

Table 5 ANOVA and Model Fitness for Biodiesel Yield Optimization

(A) Analysis of Variance (ANOVA) for Quadratic Model

Source	Sum of Squares	df	Mean Square	F-value	*p*-value	Significance
Model	268.35	14	19.17	53.98	< 0.0001	Highly significant
A – Catalyst Loading	53.85	1	53.85	151.63	< 0.0001	Significant
B – Temperature	40.63	1	40.63	114.40	< 0.0001	Significant
C – Time	50.27	1	50.27	141.55	< 0.0001	Significant
D – Molar Ratio	10.57	1	10.57	29.75	< 0.0001	Significant
AB	0.88	1	0.88	2.49	0.1370	Not significant
AC	2.34	1	2.34	6.59	0.0223	Significant
AD	33.52	1	33.52	94.40	< 0.0001	Significant
BC	5.06	1	5.06	14.26	0.0020	Significant
BD	17.39	1	17.39	48.97	< 0.0001	Significant
CD	20.25	1	20.25	57.02	< 0.0001	Significant
A^2	1.54	1	1.54	4.34	0.0560	Marginal
B^2	0.01	1	0.01	0.04	0.8421	Not significant
C^2	32.40	1	32.40	91.24	< 0.0001	Significant
D^2	1.75	1	1.75	4.94	0.0432	Significant
Residual	4.97	14	0.36			
Lack of Fit	1.77	10	0.18	0.22	0.9758	Not significant
Pure Error	3.20	4	0.80			
Total	273.32	28				

(B) Model Selection and Fit Summary

Model	Sequential *p*-value	Lack-of-Fit *p*-value	R^2	Adjusted R^2	Predicted R^2	Model Status
Linear	0.0003	0.0344	0.5321	0.4963	0.3459	Inadequate
2FI	0.0012	0.1379	0.8034	0.7805	0.6341	Acceptable
Quadratic	< 0.0001	0.9758	0.9818	0.9636	0.9444	**Selected**
Cubic	0.9411	0.8093	0.9567	0.9393	0.7936	Aliased

(C) Model Adequacy and Statistical Diagnostics

Statistical Parameter	Value	Interpretation
R^2	0.9818	Excellent model fit
Adjusted R^2	0.9636	Strong explanatory power
Predicted R^2	0.9444	High predictive reliability
Std. Deviation	0.5959	Low experimental error
Mean Response	87.81	
C.V. (%)	0.6786	High experimental precision
Adequate Precision	29.39	Adequate signal (> 4)

Significant terms were identified at $p < 0.05$. *A non-significant lack-of-fit indicates model adequacy. Adequate precision values greater than 4 confirm a satisfactory signal-to-noise ratio*

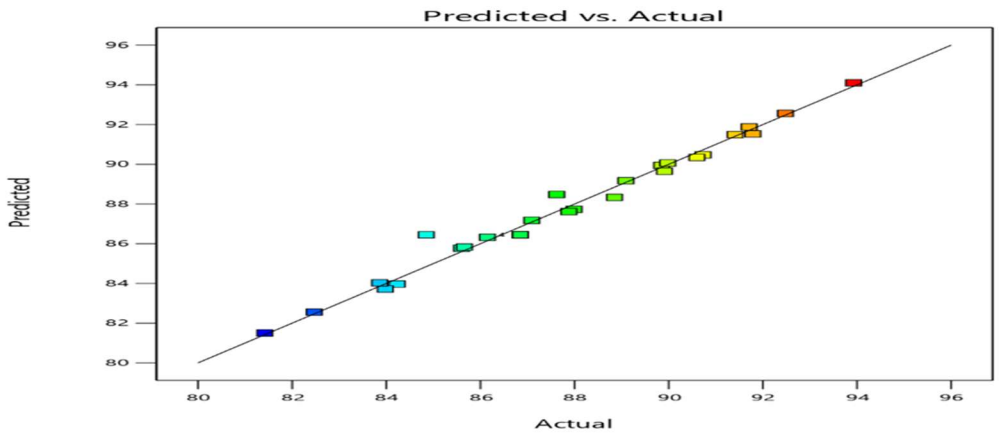

Figure 8 Predicted vs Experimental Biodiesel Yield

F. Interaction Effects of Process Variables

The 2D contour plot (Figure 9) demonstrates the synergistic interaction between reaction temperature and catalyst loading on the biodiesel yield from neem oil using CaO-based nanocatalysts. The elliptical nature of the contours indicates a statistically significant interaction ($p < 0.05$), confirming that the effect of temperature is dependent on the catalyst concentration and vice versa (Agnihotri *et al*., 2024; El-Sherif *et al*., 2023; Abo & Areti, 2025). The innermost region of the plot represents the optimal reaction conditions, typically around 55–65 °C and 1.0–2.0 wt% catalyst loading, consistent with literature on base-catalyzed transesterification of high-FFA oils (Naik *et al*., 2024; Iyya *et al*., 2024; Awogbemi *et al*., 2024).

Physicochemical analysis explains the observed trends: increasing temperature initially accelerates reaction kinetics by providing sufficient energy to overcome the activation barrier, but excessive heating (>65 °C) causes methanol evaporation, shifting equilibrium backward (Çakırca & Akın, 2021; Nabgan *et al*., 2022). Similarly, increasing catalyst loading enhances active site availability, yet overloading (>1.5–2.0 wt%) induces saponification due to free fatty acids and increases viscosity, which hinders mass transfer and lowers yield (Erchamo *et al*., 2021; Jeyakumar & Pandian, 2022; Noreen *et al*., 2021).

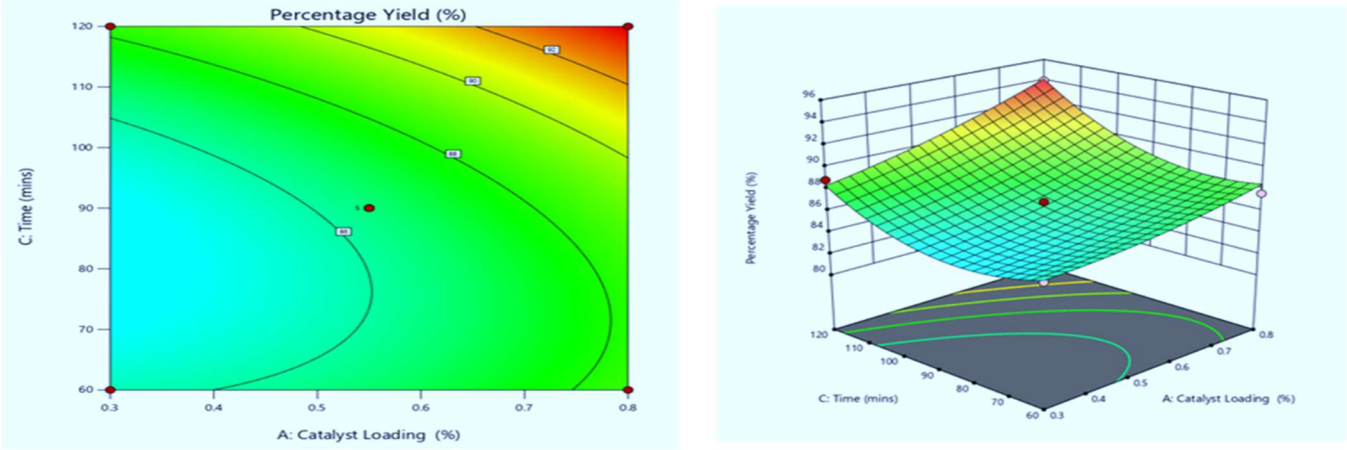

Figure 9 Contour Plot Showing the Interaction Between Reaction Temperature and Catalyst Loading

G. Biodiesel Fuel Quality Evaluation

The physicochemical characterization of neem oil biodiesel (Table 6) demonstrates compliance with ASTM D6751 standards, confirming its suitability as a sustainable diesel substitute. The density of 890 kg/m³ falls within the standard range (860–900 kg/m³), ensuring compatibility with conventional engines and fuel injection systems (Awogbemi *et al*., 2024; Erchamo *et al*., 2021). A flash point of 126 °C indicates safe handling and storage, consistent with reported values for base-catalyzed biodiesel derived from high-FFA oils (El-Sherif *et al*., 2023; Çakırca & Akın, 2021).

The cold flow properties, represented by a cloud point of 3.1 °C and a pour point of –3.5 °C, suggest satisfactory performance under moderate ambient conditions, aligning with previous findings on neem and other non-edible oil biodiesels (Iyya *et al*., 2024; Jeyakumar & Pandian, 2022). The calorific value of 39 MJ/kg exceeds the minimum ASTM requirement

(35 MJ/kg), highlighting the high energy content of the produced biodiesel (Naik *et al*., 2024; Nabgan *et al*., 2022).

The low free fatty acid content (0.51 wt%) and kinematic viscosity of 4.6 mm^2/s are indicative of effective transesterification and homogeneous methyl ester formation, critical for engine performance and injector operability (Noreen *et al*., 2021; Awogbemi *et al*., 2024). The cetane number of 52 falls comfortably within the ASTM range (47–65), ensuring efficient combustion and low ignition delay. The amber yellow color and smoke point of 93 corroborate the absence of residual glycerides and impurities, reflecting the high purity of the biodiesel (El-Sherif *et al*., 2023; Erchamo *et al*., 2021). Collectively, these properties validate that the CaO-based nanocatalyst-mediated transesterification of neem oil produces biodiesel of high physicochemical quality, consistent with international fuel standards and comparable to other non-edible oil-derived biodiesels (Agnihotri *et al*., 2024; Iyya *et al*., 2024).

Table 6 Physicochemical Properties of Neem Oil Biodiesel Compared with ASTM D6751

S/N	Property	Unit	Result Obtained	ASTM D6751 (Min)	ASTM D6751 (Max)
1	Density	Kg/m^3	890	860	900
2	Flash point	°C	126	100	170
3	Cloud point	°C	3.1	–	–
4	Pour point	°C	-3.5	-5 to 10	–
5	Colour	–	Amber yellow	–	–
6	Smoke point	–	93	–	–
7	Calorific value	MJ/kg	39	35	–
8	FFA	wt%	0.51	–	–
9	Cetane number	–	52	47	65
10	Kinematic viscosity	mm^2/s	4.6	1.9	6.0

H. Catalyst Stability and Reusability

The reusability assessment of the CaO/Metakaolinite /Fe_3O_4 nanocatalyst (Table 7) demonstrates that the catalyst maintains high activity over multiple transesterification cycles. Biodiesel yields remained above 90wt. % for the first three cycles, indicating excellent initial stability and minimal leaching of active sites. A gradual decline in yield from the fourth to the seventh cycle (87.5 wt.% to 62.0 wt.%) is observed, which is typical of heterogeneous CaO-based catalysts due to partial deactivation caused by surface fouling, active site leaching, or slight sintering under repeated reaction conditions (Erchamo *et al*., 2021; Iyya *et al*., 2024).

The sustained high yields in early cycles confirm the strong interfacial bonding between CaO and the metakaolinite support, which mitigates nanoparticle aggregation and preserves active surface area (Jeyakumar & Pandian, 2022; Naik *et al*., 2024). This performance aligns with prior studies where biogenic CaO catalysts derived from eggshells, chicken bone, or other natural sources maintained >85 wt. % conversion over 3–5 cycles before significant activity loss (Abo & Areti, 2025; Nabgan *et al*., 2022; Noreen *et al*., 2021).

The CaO/metakaolin/Fe_3O_4 catalyst shows good initial activity but limited stability upon reuse due to leaching, fouling, and structural degradation. As shown in Figure 2(b) of the N_2 adsorption–desorption isotherms of the spent 2:1:1 nanocomposite catalyst, there is a significant degradation of the spent CaO/metakaolin/Fe_3O_4 catalyst after 7 cycles, as evidenced by a significant reduction in surface area from 117 to 9.142 m^2/g and pore volume from 0.80 to 0.01132 cm^3/g. This is consistent with the deactivation of biodiesel catalysts, where there is pore blockage due to glycerol, soaps, and unreacted substances (Fronza et al., 2026). The same findings have been reported by other studies, where there is significant fouling, calcium leaching, and pore size reduction, resulting in a significant reduction of surface area and efficiency after repeated biodiesel synthesis cycles. Percentages (Suhel et al., 2025). As shown from the reduction of pore widths from 3.5 to 2.042 nm, there is a significant indication of the transition to restricted diffusion, as shown by textural degradation rather than chemical deactivation.

Table 7 Catalyst Reusability over Successive Reaction Cycles

Cycle	Biodiesel Yield (wt. %)
1	91.7
2	91.5
3	90.0
4	87.5
5	79.2
6	75.5
7	62.0

I. Engine Performance and Emission Characteristics

The performance and emission evaluation of neem oil biodiesel blends in a compression-ignition engine reveals clear trends consistent with established biodiesel combustion characteristics. Figure 10a–c and Table 8, Table 9, Table 10 provide a comprehensive overview of brake thermal efficiency (BTE), carbon monoxide (CO) emissions, and oxides of nitrogen (NOx) across various blend ratios (B0, B20, B50, B80, B100) at different engine speeds.

Brake Thermal Efficiency (BTE) increased progressively with engine speed for all tested blends. Neat diesel (B0) exhibited BTE values ranging from 7.5 ± 0.3 wt.% to 13.5 ± 0.3 wt.%, while B20 showed higher efficiency, ranging from 8.5 ± 0.3 wt.% to 15.5 ± 0.3 wt.% (Table 9a, Figure 8a). The slight

enhancement in BTE for B20 is attributable to the intrinsic 11 wt.% oxygen content in neem biodiesel, which promotes more complete combustion by facilitating oxidation in fuel-rich zones. Higher blends, such as B50, B80, and B100, exhibited further improvements in BTE, with B100 achieving a maximum of 23.5 ± 0.3 wt.% at peak engine speeds. The relatively narrow standard deviations across all blends indicate stable combustion and high measurement repeatability, confirming the reliability of the results.

CO emissions showed a declining trend with increasing biodiesel content, consistent with improved oxidation due to fuel-bound oxygen. B0 produced CO in the range of 420 ± 10 ppm to 490 ± 10 ppm, whereas B20 ranged from 410 ± 10 ppm to 480 ± 10 ppm. Higher blends further reduced CO emissions, with B100 ranging between 370 ± 10 ppm and 450 ± 10 ppm (Table 9b, Figure 8b). The consistent ±10 ppm spread across repeated trials highlights the precision and repeatability of the emission measurements. These results confirm the effectiveness of oxygenated biodiesel blends in mitigating incomplete combustion by-products.

NOx emissions increased with engine speed, reflecting the thermal-kinetic behavior of biodiesel combustion. Neat diesel (B0) ranged from 17 ± 0.5 ppm to 23 ± 0.5 ppm, while B20 exhibited slightly higher NOx values, from 16 ± 0.5 ppm to 22 ± 0.5 ppm, indicating a moderate increase under certain operating conditions (Table 9c, Figure 8c). Higher blends, including B50, B80, and B100, produced comparable or slightly elevated NOx emissions. The low standard deviation of ±0.5 ppm suggests stable combustion conditions, providing confidence in the Collectively, the results highlight that B20 offers an optimal balance between engine performance and environmental benefit. The minor increase in NOx is offset by significant reductions in CO and potential particulate formation, while BTE is maintained or slightly enhanced relative to diesel. This aligns with literature reports indicating that oxygenated biodiesel improves combustion efficiency while slightly elevating peak in-cylinder temperatures, leading to marginal NOx increases (Iyya et al., 2024; Jeyakumar & Pandian, 2022; Noreen et al., 2021).

The progressive trends observed with higher blends (B50–B100) suggest further performance gains, but with careful consideration of potential NOx rise. Overall, neem oil biodiesel blends demonstrate sustainable compatibility with conventional diesel engines, providing a pathway toward reduced carbonaceous emissions without compromising thermal efficiency

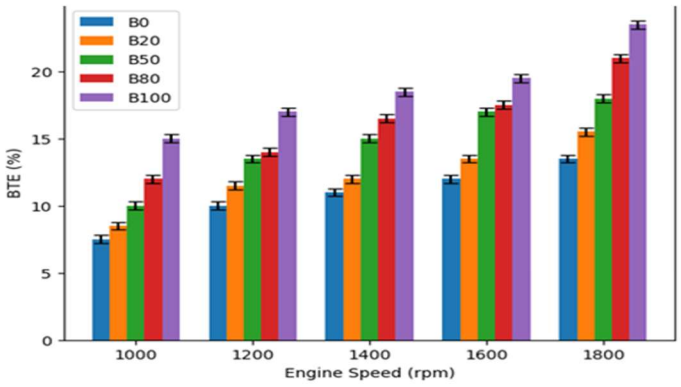

(A): Variation of Brake Thermal Efficiency (BTE) with engine speed for neem oil biodiesel blends, showing improved efficiency with increasing biodiesel proportion. Error bars represent mean ± standard deviation.

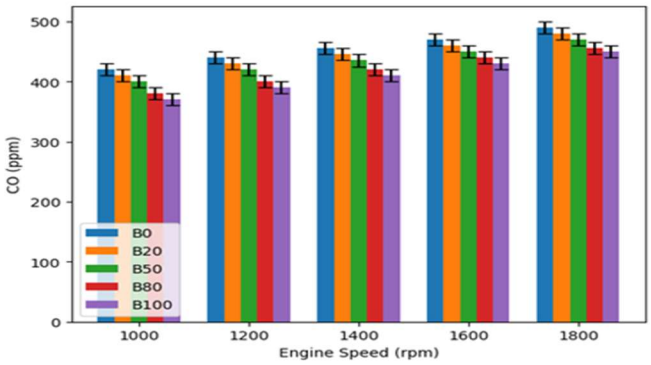

(B): Variation of carbon monoxide (CO) emissions with engine speed, indicating a reduction in emissions with increasing biodiesel content. Error bars represent mean ± standard deviation.

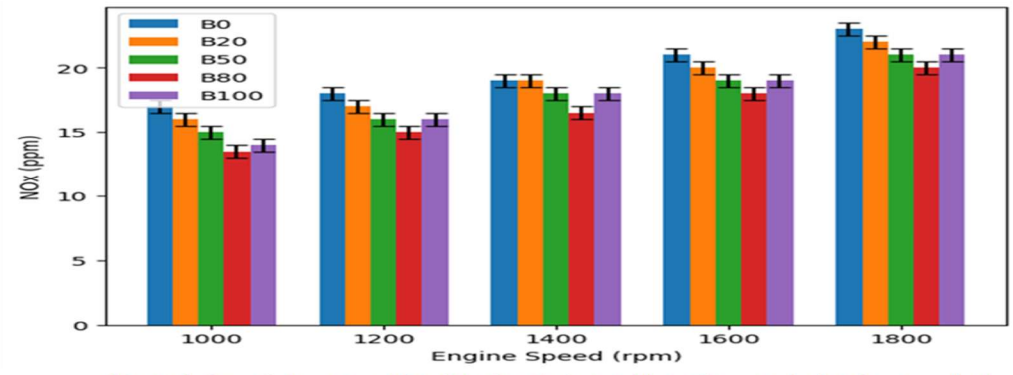

(C): Variation of nitrogen oxides (NOx) emissions with engine speed, showing a gradual increase with higher biodiesel blends. Error bars represent mean ± standard deviation.

Figure 10. Engine Performance and Emission Comparison of B20 Biodiesel and Conventional Diesel Fuel

Table 8 Brake Thermal Efficiency (BTE)

Speed (rpm)	B0 (wt. %)	B20 (wt. %)	B50 (wt. %)	B80 (wt.%)	B100 (wt.%)
1000	7.5 ± 0.3	8.5 ± 0.3	10.0 ± 0.3	12.0 ± 0.3	15.0 ± 0.3
1200	10.0 ± 0.3	11.5 ± 0.3	13.5 ± 0.3	14.0 ± 0.3	17.0 ± 0.3
1400	11.0 ± 0.3	12.0 ± 0.3	15.0 ± 0.3	16.5 ± 0.3	18.5 ± 0.3
1600	12.0 ± 0.3	13.5 ± 0.3	17.0 ± 0.3	17.5 ± 0.3	19.5 ± 0.3
1800	13.5 ± 0.3	15.5 ± 0.3	18.0 ± 0.3	21.0 ± 0.3	23.5 ± 0.3

Table 9 CO Emissions

Speed (rpm)	B0 (ppm)	B20 (ppm)	B50 (ppm)	B80 (ppm)	B100 (ppm)
1000	420 ± 10	410 ± 10	400 ± 10	380 ± 10	370 ± 10
1200	440 ± 10	430 ± 10	420 ± 10	400 ± 10	390 ± 10
1400	455 ± 10	445 ± 10	435 ± 10	420 ± 10	410 ± 10
1600	470 ± 10	460 ± 10	450 ± 10	440 ± 10	430 ± 10
1800	490 ± 10	480 ± 10	470 ± 10	455 ± 10	450 ± 10

Table 10 NOx Emissions

Speed (rpm)	B0 (ppm)	B20 (ppm)	B50 (ppm)	B80 (ppm)	B100 (ppm)
1000	17 ± 0.5	16 ± 0.5	15 ± 0.5	13.5 ± 0.5	14 ± 0.5
1200	18 ± 0.5	17 ± 0.5	16 ± 0.5	15 ± 0.5	16 ± 0.5
1400	19 ± 0.5	19 ± 0.5	18 ± 0.5	16.5 ± 0.5	18 ± 0.5
1600	21 ± 0.5	20 ± 0.5	19 ± 0.5	18 ± 0.5	19 ± 0.5
1800	23 ± 0.5	22 ± 0.5	21 ± 0.5	20 ± 0.5	21 ± 0.5

Table 11 presents a comparative analysis of various catalyst systems employed for biodiesel production. It summarizes the feedstocks used, key strengths or advantages, and limitations of each catalyst, highlighting their performance in terms of biodiesel yield, reusability, and process efficiency. The table also emphasizes recent advancements, particularly the development of magnetic and nanocomposite catalysts, which address common challenges such as leaching, low reusability, and complex recovery processes. The final entry showcases the current study's catalyst system, which integrates low-cost, waste-derived materials with magnetic recovery, optimizing both efficiency and sustainability.

Table 11 Comparative analysis of various catalyst systems

S/N	Catalyst System	Feedstock	Key Findings / Strengths	Limitations Identified	Reference
1	Pure CaO (eggshell-derived)	Waste oil / lard	High basicity and good catalytic activity; biodiesel yields up to 90 wt.% under optimized conditions; low-cost and readily available	Prone to leaching, low reusability, sensitivity to moisture and CO_2; reduced activity after repeated cycles	Raiedhah et al ., 2023
2	Modified CaO (ZnO/TiO_2 supported)	Waste cooking oil	Improved surface area and catalytic efficiency; biodiesel yield increased to 95 wt.% compared to 80 wt.% for pure CaO	More complex synthesis route; limited magnetic recovery and separation challenges	Welela et al., 2021
3	$CaO–ZnCO_2O_4$ nanocomposite	Model oil (tributyrin)	Enhanced catalytic activity due to synergistic interaction; increased number of active sites and improved stability compared to single CaO	Does not address catalyst recovery; limited application to real feedstocks	Katabathini et al., 2023
4	$CaO–CeO_2$ composite (RSM optimized)	Non-edible seed oil	Very high biodiesel yield (98 wt.%); improved dispersion, porosity, and process optimization efficiency	Use of expensive rare-earth dopant (CeO_2); lacks magnetic separability; scalability concerns	Biru et al., 2026

5	Magnetic CaO-based composites (CaO/Zeolite/Fe_3O_4 or CaO/MgO/Fe_3O_4)	Waste cooking oil	Magnetic recovery capability; high biodiesel yield (91 wt.%); good reusability (up to 4 cycles); enhanced stability and surface area	Multi-step synthesis; higher material cost due to supports like zeolite; possible agglomeration of magnetic particles	Widayat et al., 2024
6	Nano CaO / Metakaolinite / Magnetite (This Study)	Neem oil (non-edible)	Integration of waste-derived CaO, low-cost metakaolinite support, and magnetic Fe_3O_4; improved dispersion and surface area; easy magnetic recovery; enhanced reusability and cost-effectiveness; optimization ensures maximum biodiesel yield	Minimal research gap: combines low-cost support, magnetic recovery, and waste valorization in a single system; addresses major limitations of prior catalysts simultaneously	This Work (2026)

V CONCLUSION

Researchers created a sustainable waste-based magnetic CaO/Metakaolinite/Fe_3O_4 nanocomposite catalyst which they used successfully to produce biodiesel from non-edible neem oil. The hybrid catalyst achieved structural synergy through the combination of eggshell CaO, Kutigi kaolin metakaolinite, and plant-based Fe_3O_4, which produced a catalyst that exhibited high basicity and improved surface area and mesoporosity and exceptional magnetic properties. The complete analysis of physicochemical properties proved that active CaO sites distributed evenly throughout the material while the crystalline structures of CaO and Fe_3O_4 remained intact and metakaolinite support material protected against particle agglomeration and sintering. The Box–Behnken response surface methodology process optimization study confirmed complete model validity with accurate prediction capabilities which produced biodiesel conversion rates above 90 wt.% under mild reaction conditions. The produced neem oil biodiesel met all key ASTM D6751 specifications which showed high fuel quality and effective transesterification because the feedstock contained high free-fatty-acid content. The catalyst showed practical benefits during reusability tests because magnetic separation allowed easy recovery of approximately 62 wt.% activity after seven cycles, which demonstrated its stability during operations and its potential to generate economic benefits. The engine performance tests showed that B20 biodiesel blends achieved diesel-like brake thermal efficiency, while they produced lower CO and HC and particulate emissions, although they released slightly more NO_x, which follows normal biodiesel combustion patterns. The research results show that neem oil biodiesel provides environmental advantages which make it suitable to replace part of diesel fuel in compression-ignition engines. The CaO/Metakaolinite/Fe_3O_4 nanocomposite catalyst which we developed functions as a scalable solution which produces biodiesel from non-edible oils at low expenses while maintaining safe environmental practices. The project uses local waste materials to produce green synthesis materials which enable magnetic recovery processes that support both circular economy practices and sustainable energy methods. The research work makes a major contribution to developing new heterogeneous catalysts for renewable fuel production while creating an effective pathway which leads to environmentally friendly biodiesel technologies that countries can use in their large-scale operations.

AUTHOR CONTRIBUTIONS

Amina Nwokedi: Investigation, Methodology, Writing – original draft and editing.
Akpan Uduak George: Conceptualization and Supervision
Olutoye Moses Aderemi: Conceptualization, Supervision and Editing
DIM, Paul Egwuonwu: Supervision and editing

ACKNOWLEDGEMENT

The authors would like to thank the Federal University of Technology Minna, Nigeria for providing access to essential resources although not based on financial ground.

REFERENCES

Abo, L.D.; H.A. Areti. (2025). Advancements in heterogeneous biobased and bio-composite catalysts: A comprehensive review on synthesis, characterizations, and applications in biodiesel production. BioEnergy Research, 18(1), pp.68–85.

Akatobi, K.N. (2024). Synthesis and characterisation of CaO nanoparticle from oyster shell using sol–gel method. LAUTECH Journal of Engineering and Technology, pp.101–109.

Awogbemi, O.; A.A. Ojo and S.A. Adeleye. (2024). Advancements in the application of metal oxide nanocatalysts for sustainable biodiesel production. Discover Applied Sciences, 6(5), p.250.

Biru, B.; D. Devendra; H. Tigabu and Y. Kumlachew. (2025). RSM-optimized biodiesel production from Ethiopian Podocarpus falcatus seed oil using a CaO-CeO2 heterogeneous composite catalyst and oxidative stability assessment. Scientific Reports, volume 16, Article number: 3919.

Çakırca, E.E.; A.N. Akın. (2021). Study on heterogeneous catalysts from calcined Ca-riched hydrotalcite-like compounds for biodiesel production. Sustainable Chemistry and Pharmacy, 20, 100378.

de Jesus Andrade Fidelis, R.; M. Pires; D.S. de Resende; G.F. Costa Lima; P.R.P. de Paiva and A.C. da S. Bezerra. (2025). Magnetite: Properties and applications – A review. Journal of Magnetism and Magnetic Materials, 614, 172770. https://doi.org/https://doi.org/10.1016/j.jmmm.2025.172770

El-Sherif, A.A.; A.M. Hamad; E. Shams-Eldin; H.A.A.E. Mohamed; A.M. Ahmed; M.A. Mohamed; H.M. Abdelrahman and H.M. Fahmy. (2023). Power of recycling waste cooking oil into biodiesel via green CaO-based eggshells/Ag heterogeneous nanocatalyst. Renewable Energy, 202, pp.1412–1423.

Erchamo, Y.S.; T.T. Mamo; G.A. Workneh and Y.S. Mekonnen. (2021). Improved biodiesel production from waste cooking oil with mixed methanol–ethanol using enhanced eggshell-derived CaO nano-catalyst. Scientific Reports, 11(1), p.6708.

Fronza, C.S.; H. Enzweiler and N.P.G. Salau. (2026). Valorization of biodiesel-derived glycerol into fuel additives: advances in esterification, etherification, and ketalization using sulfonated catalysts. Fuel, 420, 138867. https://doi.org/https://doi.org/10.1016/j.fuel.2026.138867

Iyya, Z.; S. Saidu; N. Mohmmed; M. Shaibu and A. Rufai. (2024). Sustainable production of bio-lubricants from neem seed oil using eggshell-derived calcium oxide catalyst. International Journal of Trend Research in Engineering and Technology, 8, pp.42–49.

Jeyakumar, N.; P.L. Pandian. (2022). Yield enhancement of Azadirachta indica biodiesel employing calcium oxide catalyst derived from chicken bone waste. AIP Conference Proceedings, 2653(1), 040002.

Katabathini, N.; M.Z. Mohamed and B. Wejdan. (2023). Mechanochemical synthesized CaO/ZnCO2O4 Nanocomposite for Biodiesel production. Catalyst, 13(2), 398. https://doi.org/10.3390/catal13020398

Koo, K.N.; A.F. Ismail; M.H.D. Othman; M.A. Rahman and T.Z. Sheng. (2019). Preparation and characterization of superparamagnetic magnetite (Fe3O4) nanoparticles: A short review. Malaysian Journal of Fundamental and Applied Sciences, 15(1), 23–31. https://doi.org/10.11113/mjfas.v15n2019.1224

Linganiso, E.C.; B. Tlhaole; L.P. Magagula; S. Dziike; L.Z. Linganiso; T.E. Motaung; N. Moloto and Z.N. Tetana. (2022). Biodiesel production from waste oils: A South African outlook. Sustainability, 14(4), 41983.

Liu, C.C.; S. Sadhasivam; S. Savitha and F.H. Lin. (2014). Fabrication of multiwalled carbon nanotubes–magnetite nanocomposite as an effective ultra-sensing platform for the early screening of nasopharyngeal carcinoma by luminescence immunoassay. Talanta, 122, pp.195–200.

Long, F.; W. Liu; X. Jiang; Q. Zhai; X. Cao; J. Jiang and J. Xu. (2021). State-of-the-art technologies for biofuel production from triglycerides: A review. Renewable and Sustainable Energy Reviews, 148, 111269.

Nabgan, W.; A.A. Jalil; B. Nabgan; A.H. Jadhav; M. Ikram; A. Ul-Hamid and N.S. Hassan. (2022). Sustainable biodiesel generation through catalytic transesterification of waste sources: A literature review and bibliometric survey. RSC Advances, 12(3), pp.1604–1627.

Naik, N.S.; S. Divakar; J.M.S. Budagumpi; R.G. Balakrishna and M. Padaki. (2024). Biogenic derived eggshell and its derivatives as solid base heterogeneous catalysts for organic transformations: A comprehensive review. RSC Sustainability, 2(5), pp.1246–1268.

Nguyen, H.C.; M.L. Nguyen; C.H. Su; H.C. Ong; H.Y. Juan and S.J. Wu. (2021). Bio-derived catalysts: A current trend of catalysts used in biodiesel production. Catalysts, 11(7), p.812.

Noreen, S.; K. Khalid; M. Iqbal; H.B. Baghdadi; N. Nisar; U.H. Siddiqua; J. Nisar; Y. Slimani; M.I. Khan and A. Nazir. (2021). Eco-benign approach to produce biodiesel from neem oil using heterogeneous nano-catalysts and process optimization. Environmental Technology & Innovation, 22, 101430.

Paredes-Quevedo, L.C.; C. Batiot-Dupeyrat and M. Velasquez. (2025). Catalytic performance of Cu–Co/metakaolinite: Role of textural and structural properties in the partial oxidation of glycerol. Materials Advances, 6(11), pp.3512–3522.

Rahmayanti, M.; I. Fatimah; A.Y. Ikhsani and D.N. Azizah. (2024). The potential of calcium oxide nanocatalyst from chicken eggshells for biodiesel production using chicken fat waste. Inorganic Chemistry Communications, 165, 112604.

Raiedhah, A.A.; M.M. Esraa and A. Moustafa. (2023). Effects of calcination temperature of eggshell-derived CaO as a catalyst for biodiesel production from waste cooking oil. South African Journal of Chemistry, vol.77. https://doi.org/10.17159/0379-4350/2023/v77a05

Rehman, N.; F. Haq and S. Faisal. (2023). Phytochemical analysis and antioxidant potential of Calotropis procera and Calotropis gigantea. Asian Journal of Biological Sciences, 16(3), pp.254–263.

Saleem, M.; F. Jamil; O.A. Qamar; P. Akhter; M. Hussain; M.S. Khurram; A.A.H. Al-Muhtaseb; A. Inayat and N.S. Shah. (2022). Enhancing the catalytic activity of eggshell-derived CaO catalyst and its application in biodiesel production from waste chicken fat. Catalysts, 12(12), 1627.

Salgado Mendoza, P.; K. Márquez; O. Rubilar and D. Contreras. (2018). The effect of phenolic compounds on the green synthesis of iron nanoparticles (FexOy-NPs) with photocatalytic activity. Applied Nanoscience, 9, pp.459–470.

Sathiyamoorthi, E.; J. Lee; M.D. Ramesh; N.D. Nguyen and R. Shanmuganathan. (2024). Biodiesel production from eggshells derived bio-nano CaO catalyst – Microemulsion fuel blends for up-gradation of biodiesel. Environmental Research, 260, 119626.

Suhel, A.; N. Abdul Rahim; M.R. Abdul Rahman and K.A. Bin Ahmad. (2025). Biodiesel synthesis from waste animal fat using waste chicken eggshells derived heterogeneous catalysts: An optimization study through Taguchi model. Results in Engineering, 28, 107261. https://doi.org/https://doi.org/10.1016/j.rineng.2025.107261

Welela, M.K.; T.W. Kokob and S.W. Getabalew. (2023). Optimization and characterization of biodiesel from waste cooking oil using modified CaO catalyst derived from snail shell. Heliyon, 9(5):e16475. doi: 10.1016/j.heliyon.2023.e16475

Widayat, H.S.; W.S. Prambudi; S. Dimas; B. Luqman; H. Hadiyanto and A.N. Faustina. (2024). Preparation CaO/MgO/Fe3O4 magnetite catalyst and catalytic test for biodiesel production Research gate, Vol. 22 p. 102202. https://doi.org/10.1016/j.rineng.2024.102202

Zhang, M.; G. Ramya; K. Brindhadevi; M. Alsehli; A. Elfasakhany; C. Xia; S.T. Huang and A. Pugazhendhi. (2022). Microwave-assisted biodiesel production from chicken feather meal oil using bio-nano calcium oxide derived from chicken eggshell. Environmental Research, 205, 112509

.